

# *Chandra* Observations of Gravitational Lenses B1600+434 and B1608+656

Xinyu Dai<sup>1</sup> and Christopher S. Kochanek<sup>1</sup>

## ABSTRACT

We observed B1600+434 and B1608+656 with CXO/ACIS, detecting both quasar images in B1600+434 and three of four images in B1608+656. We did not detect significant X-ray emission from nearby galaxy groups or clusters associated with each lens galaxy. The upper limits on the X-ray luminosity of any cluster within  $4'$  of each lens and at each lens redshift are of  $\sim 2 \times 10^{42}$  and  $\sim 6 \times 10^{42}$  erg s<sup>-1</sup> for B1600+434 and B1608+656, respectively. The radio-loud source quasars have power-law photon indices of  $\Gamma = 1.9 \pm 0.2$  and  $\Gamma = 1.4 \pm 0.3$  and X-ray luminosities of  $1.4_{-0.1}^{+0.2} \times 10^{45}$  and  $2.9_{-0.4}^{+0.7} \times 10^{44}$  erg s<sup>-1</sup> for B1600+434 and B1608+656, respectively before correcting for the magnification. We detected a differential absorption column density of  $\Delta N_{\text{H}} \sim 3 \times 10^{21}$  cm<sup>-2</sup> between the two images of B1600+434, roughly consistent with expectations from differential extinction estimates of  $\Delta E(B - V) = 0.1$  mag and a standard dust-to-gas ratio. The differential absorption observed in gravitational lenses may serve as an important probe to study the gas content in high redshift galaxies since it can separate the absorbing column originating from the lens galaxy and those intrinsic to quasars. We also detected 157 serendipitous X-ray sources in the two *Chandra* fields and identified the brighter optical counterparts using the SDSS and DPOSS surveys.

*Subject headings:* gravitational lensing

## 1. Introduction

The radio-loud gravitational lenses B1600+434 and B1608+656 were discovered in the Cosmic Lens All Sky Survey (Jackson et al. 1995; Myers et al. 1995). B1608+656 was also discovered independently by Snellen et al. (1995). B1600+434 is a two image system

---

<sup>1</sup>Department of Astronomy, The Ohio State University, Columbus, OH 43210, xinyu@astronomy.ohio-state.edu, ckochanek@astronomy.ohio-state.edu

separated by  $1''.4$  with source redshift  $z = 1.59$  (Jackson et al. 1995; Fassnacht & Cohen 1998). The lens galaxy of B1600+434 is an edge-on early-type spiral galaxy at  $z = 0.41$  (Jaunsen & Hjorth 1997; Fassnacht & Cohen 1998). B1608+656 is a four image system about  $2''.1$  across with a source redshift at  $z = 1.39$  (Fassnacht et al. 1996) and a lens redshift at  $z = 0.63$  (Myers et al. 1995). The lens of B1608+656 consists of two interacting elliptical galaxies within the Einstein ring. In addition, *HST* observations have detected extended images of the AGN host galaxies in both systems (Jackson et al. 1998; Kochanek et al. 1999; Kochanek, Keeton, & McLeod 2001; Surpi & Blandford 2003).

One of the important applications of gravitational lenses is to constrain the Hubble constant (Refsdal 1964) or alternatively, the dark matter distribution in the lens galaxy, through time-delay measurements between the lensed images. The time-delays in both B1600+434 and B1608+656 have been measured (Fassnacht et al. 1999, 2002; Koopmans et al. 2000; Burud et al. 2000). Modeling of the two gravitational lenses has been carried out by several studies (e.g., Koopmans & Fassnacht 1999; Koopmans et al. 2003; Kochanek 2002, 2003). In most studies, there are model degeneracy problems in that a number of models can reproduce the limited number of constraints and predict different Hubble constant values based on each time delay measurement. Therefore, it is important to map the mass distribution close to the lens galaxy with other independent methods to better constrain the lens models. In many lenses, galaxy groups or clusters close to the lenses provide non-negligible contribution to the lens potential (Keeton & Zabludoff 2004; Fassnacht & Lubin 2002). X-ray observations are particularly important in this respect because they can accurately constrain the positions and masses of the galaxy groups or clusters. In particular, the centroid of the X-ray emission from the intracluster gas provides a more accurate measurement of the cluster’s position than optical studies. X-ray clusters or groups have been observed in the lenses RX J0911.4+0551, Q0957+561, B1422+231, and PG 1115+080 (Morgan et al. 2001; Chartas et al. 2002c; Raychaudhury, Saha, & Williams 2003; Grant et al. 2004).

The superb angular resolution of *Chandra* also allows us to resolve the lensed quasar images if they are separated by more than  $0''.5$ . Thus, besides constraining the properties of galaxy groups or clusters, X-ray observations of gravitational lenses can also be used to constrain the sizes of quasar X-ray emission regions (Dai et al. 2003; Chartas et al. 2002a, 2004), to measure ultra-short time delays between lensed images (Chartas et al. 2001; Dai et al. 2003; Chartas, Dai, & Garmire 2004), and to study the interstellar medium of the lens galaxies (e.g., Dai et al. 2003). In addition, the flux magnification provided by gravitational lensing facilitates studies of objects that are intrinsically X-ray faint, such as broad absorption line quasars (Chartas et al. 2002b; Gallagher et al. 2002) and high redshift quasars (Dai et al. 2004).

In this paper, we present results from *Chandra* observations of B1600+434 and B1608+656. We discuss the data acquisition and processing in §2, the spectral properties of the lensed quasars in §3, our limits on the presence of X-ray luminous groups or clusters in §4, and the serendipitous sources in the fields in §5. We assume cosmology with  $H_0 = 70 \text{ km s}^{-1} \text{ Mpc}^{-1}$ ,  $\Omega_m = 0.3$ , and  $\Omega_\Lambda = 0.7$  throughout the paper.

## 2. Observations and Data Reduction

We observed B1600+434 and B1608+656 with the Advanced CCD Imaging Spectrometer (ACIS; Garmire et al. 2003) onboard *Chandra* (Weisskopf et al. 2002) for  $\sim 30.2$  ks and  $\sim 29.7$  ks on 2003 October 7, and 2003 September 21, respectively. The data were taken continuously with no interruptions during each observation, and there were no significant background flares during the observations. Both gravitational lenses were placed on the back-illuminated ACIS-S3 chip, where the aim points of the observations are located, and the data were taken in the TIMED/VFAINT mode. B1600+434 was placed near the aim point of the observation ( $\sim 8''$  off-axis) and B1608+656 was placed much further from the aim point about  $\sim 75''$  off-axis. The latter lens was shifted off-axis to ensure a galaxy clump in the *HST* images would stay in the field. This configuration was used to maximize the sensitivity for detecting nearby galaxy groups or clusters that might contribute to the lensing and affect estimates of the Hubble constant. The data were reduced with the CIAO 3.1 software tools provided by the *Chandra X-ray Center* (CXC). We improved the image quality of the data by removing the pixel randomization applied to the event positions in the CXC processing and by applying a subpixel resolution technique (Tsunemi et al. 2001; Mori et al. 2001). In the data analysis, only events with standard *ASCA* grades of 0, 2, 3, 4, and 6 were used.

## 3. Lensed Quasars

We first discuss the X-ray properties of the lensed quasars in both lens systems. The imaging and spectral analysis are discussed in §3.1 and §3.2 and the X-ray flux ratios of the lensed images are estimated in §3.3.

### 3.1. Imaging Analysis

We analyzed images limited to the 0.2–8 keV band where we detected a total of 332 and 84 net events for B1600+434 and B1608+656, respectively. The raw and smoothed *Chandra*

images of B1600+434 and B1608+656 are shown in Figure 1. Both of the raw images are binned with a bin size of  $0''.15$ . The smoothed images are generated by binning the images with a bin size of  $0''.1$  for both lenses and then were smoothed with Gaussians of width  $\sigma = 0''.2$  and  $\sigma = 0''.3$  for B1600+434 and B1608+656, respectively.

In B1600+434 we detected both lensed images. The measured image separation ( $1''.35 \pm 0''.05$ ) is consistent with the separation measured in the CfA-Arizona Space Telescope LENS Survey (CASTLES) *HST* observations.<sup>1</sup>

The situation is more complicated in B1608+656 due to the large number of images with smaller minimum separations, but also because the count rate of the lens is lower. The relatively larger off-axis angle does not degrade the point spread function (PSF) very much. We simulated the PSF using the **ChART** (Carter et al. 2003) and **MARX** (Wise et al. 1997) tools and found the 50% encircled energy contour is of  $\sim 0''.5$  radius as opposed to  $\sim 0''.4$  on axis. Three out of four lensed images are clearly detected. Image B is well separated, but images A and C are merged. We fit the image assuming there are three point images of A, B, and C constraining the relative quasar position to match the CASTLES *H*-band relative position and using the above mentioned PSF model. However, we are unable to obtain a stable solution. This may be due to the low count-rate of the source or it may indicate that the images are not point sources. We note that there are some X-ray events about  $1''$  Northwest to image A and we are unable to determine whether these events belong to image A or from other unidentified sources. The *HST* images do not show any source at the corresponding position other than part of the Einstein ring image of the host galaxy. Image D is not detected by the *Chandra* observation. The non-detection of image D could be caused by small number statistics – additional absorption is not required to mask the image.

### 3.2. Spectral Analysis

We extracted spectra for each quasar using the CIAO tool **psextract** and fit them using **XSPEC V11.3.1** (Arnaud 1996) within the 0.4–8 keV observed energy range. We note that in CIAO 3.1 the recently observed decline in the low energy quantum efficiency of ACIS, possibly caused by molecular contamination of the ACIS filters, is already accounted for by the **psextract** tool. Therefore, we did not perform any other corrections beyond that.

---

<sup>1</sup>The CASTLES website is located at <http://cfa-www.harvard.edu/castles/>.

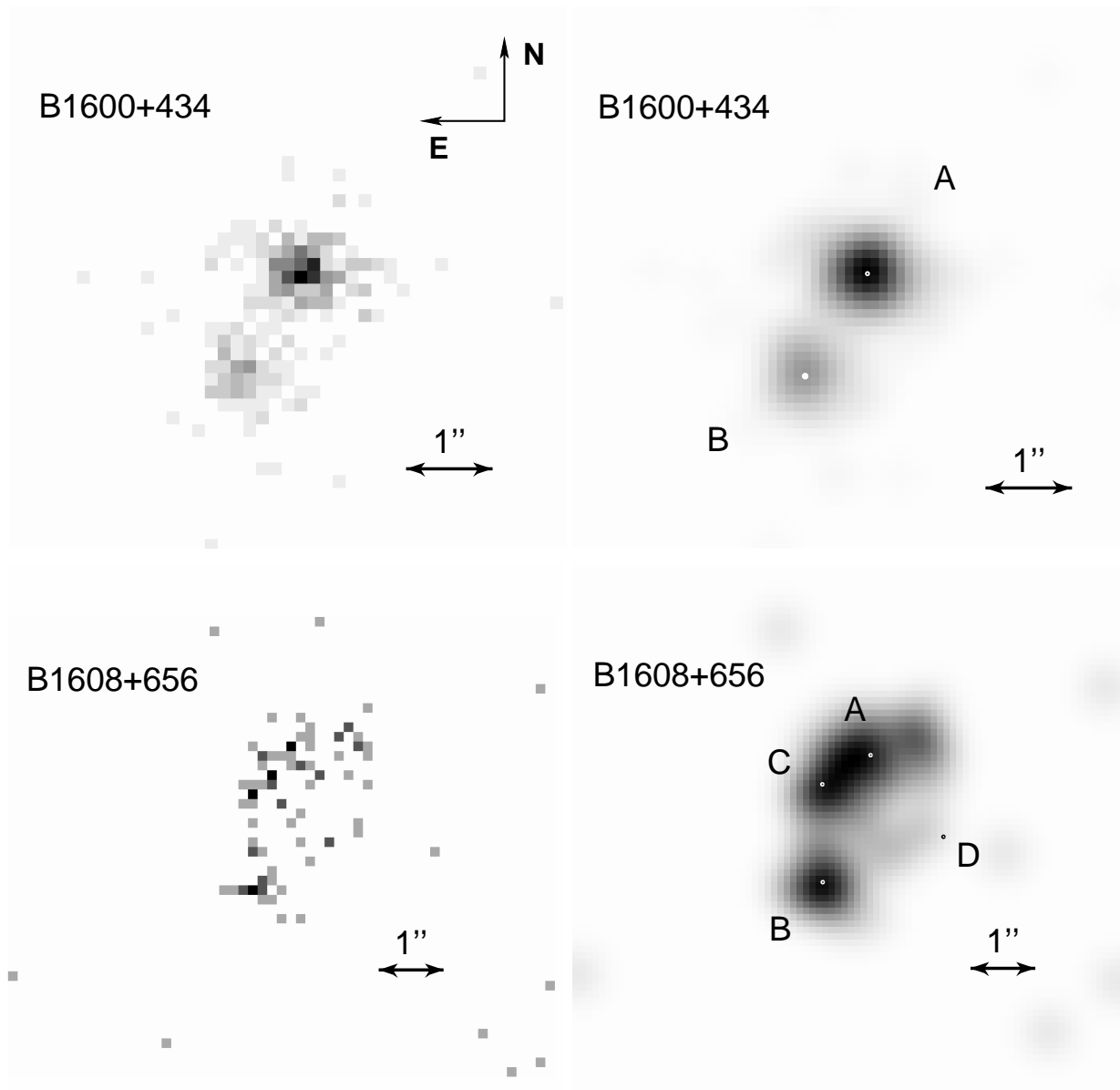


Fig. 1.— In the left panel we show the raw images of B1600+434 (top) and B1608+656 (bottom) with the events binned in  $0''.15$  bins. In the right panel we have smoothed the images with an  $0''.2$  Gaussian for B1600+434 (top) and an  $0''.3$  Gaussian for B1608+656 (bottom). The small circles in the smoothed images show the image positions measured from the CASTLES *HST* images of the systems. The scales of the smoothed and unsmoothed images are the same. We note that the  $75''$  off-axis angle of B1608+656 observation does not affect the image analysis as the 50% encircled energy contour is of  $0''.5$  radius as opposed to  $0''.4$  on-axis.

### 3.2.1. B1600+434

We extracted both the combined spectrum of both images within a circle with  $5''$  radius about the centroid of the combined image and individual spectra of images within  $0.7''$  radius circles about the centroids of images A and B, respectively. We extracted the background spectrum within an annulus with inner and outer radii of  $10''$  and  $30''$ . We fitted the spectra of B1600+434 with a series of models summarized in Table 1. We first modeled the spectrum as a power-law modified by Galactic absorption. This model gives a reasonable fit with  $\chi^2 = 16.3$  for 18 degrees of freedom (dof). However, the column density obtained for Galactic absorption,  $N_{\text{H}} = (14 \pm 4) \times 10^{20} \text{ cm}^{-2}$ , is much higher than the expected  $N_{\text{H}} = 1.3 \times 10^{20} \text{ cm}^{-2}$  (Dickey & Lockman 1990). This exercise indicates that additional absorption components are needed to interpret the spectrum. These additional absorption components can be either intrinsic to the quasar, located in the quasar host galaxy, or in the lens galaxy. We found that adding a neutral absorption component at the redshift of either the quasar or the lens can produce an acceptable fit with  $\chi^2 = 16.1$  for 18 dof and  $\chi^2 = 15.8$  for 18 dof, respectively, for absorption at the quasar and lens redshifts. The absorption column densities obtained are  $N_{\text{H}} = (90 \pm 40) \times 10^{20} \text{ cm}^{-2}$  and  $N_{\text{H}} = (22 \pm 8) \times 10^{20} \text{ cm}^{-2}$  for absorption at the quasar or lens redshift, respectively. The combined spectrum and the best fit model with absorption at the lens redshift are shown in Figure 2a. The estimate of the intrinsic photon index is around  $\Gamma \sim 1.9$  for both models with observed 0.4–8 keV band flux of  $6.9_{-1.1}^{+0.7} \times 10^{-14} \text{ erg cm}^{-2} \text{ s}^{-1}$ , and lensed, unabsorbed X-ray luminosities in the 2–10 keV and 1–20 keV band rest frame of  $7.6_{-0.2}^{+1.6} \times 10^{44}$  and  $1.4_{-0.1}^{+0.2} \times 10^{45} \text{ erg s}^{-1}$ , respectively. We note that the lensing magnification must be included in order to obtain the unlensed luminosity.

Falco et al. (1999) interpreted the wavelength dependence of the image flux ratios as due to  $\Delta E(B - V) = 0.1$  of differential extinction obscuring image B. We also see in the spectra of the image that image B has proportionally less soft X-ray emission so that differential absorption must be intrinsic to the lens. To estimate this differential absorption we simultaneously fit the individual spectra of images A and B constrained to have the same intrinsic power-law photon index and Galactic absorption column density but allowed to have different absorption column densities at the redshift of the lens. The best fit model is shown in Figure 2b. This model also results in acceptable fit with a  $\chi^2 = 13.1$  for 12 dof as compared to  $\chi^2 = 16.4$  for 13 dof if we do not allow for differential absorption. The improvement of the fit by allowing for differential absorption is significant at the 90% confidence level according to the F-test<sup>2</sup> indicating that the X-ray data are consistent with,

---

<sup>2</sup>We did not probe the boundary of the parameter space, where the F-test fails to apply (Protassov et al. 2002).

but do not require, column density variations. The photon index obtained in this fit is slightly steeper than for the previous fits in part because the small extraction regions used to obtain individual spectra of the images to the loss of some hard X-ray photons. The absorption column densities at the lens for images A and B are  $N_{\text{H}} = (21 \pm 11) \times 10^{20} \text{ cm}^{-2}$  and  $N_{\text{H}} = 47_{-17}^{+21} \times 10^{20} \text{ cm}^{-2}$ , respectively, and the differential absorption between the two images is  $\Delta N_{\text{H}} \sim 3 \times 10^{21} \text{ cm}^{-2}$  as shown in Figure 3. This indicates that the  $N_{\text{H}}$  determined from the two spectra are different at the 90% confidence level with higher  $N_{\text{H}}$  for image B. This is consistent with the lens configuration, where the lens galaxy is much closer to image B than to image A. Comparing with the estimated differential extinction of  $\Delta E(B - V) = 0.1 \text{ mag}$  between images A and B (Falco et al. 1999), we obtained a dust-to-gas ratio of  $2.6_{-1.5}^{+1.9} \times 10^{22} \text{ mag}^{-1} \text{ cm}^{-2}$  within a factor of five from the Galactic value,  $5.8 \times 10^{21} \text{ mag}^{-1} \text{ cm}^{-2}$  (Bohlin, Savage & Drake 1978).

### 3.2.2. B1608+656

We extracted the combined spectrum of all the images of B1608+656 within a  $5''$  radius circle centered on the source. We extracted the background spectrum within an annulus with inner and outer radii of  $10''$  and  $18''$ . The background subtracted spectrum consists of only 86 net events with a count-rate of  $2.9 \times 10^{-3} \text{ count s}^{-1}$ , making a spectral analysis of the individual images impossible. We modeled the spectrum with a power-law modified by Galactic absorption. This simple model fits the spectrum quite well, with  $\chi^2 = 3.3$  for 3 dof. The parameters are presented in Table 1 and the spectrum and the best fit model are shown in Figure 2c. The power-law photon index and Galactic  $N_{\text{H}}$  are constrained to be  $\Gamma = 1.4 \pm 0.3$  and  $N_{\text{H}} < 6.4 \times 10^{20} \text{ cm}^{-2}$  consistent with the expected Galactic column density of  $N_{\text{H}} = 2.7 \times 10^{20} \text{ cm}^{-2}$  (Dickey & Lockman 1990). If we fix the Galactic absorption to this value the fits are consistent with no additional absorption at either the lens or quasar redshift with upper limits on absorption column of  $N_{\text{H}} < 10^{21}$  and  $< 2 \times 10^{21} \text{ cm}^{-2}$  at the redshift of lens or quasar, respectively. There is differential extinction in B1608+656 as well, but it is most significant for image D which we failed to detect. Our upper limit on the flux of D is not strong enough to estimate a dust-to-gas ratio. The X-ray flux in the observed 0.4–8 keV band is  $2.3 \pm 0.5 \times 10^{-14} \text{ erg cm}^{-2} \text{ s}^{-1}$ , and the lensed, unabsorbed X-ray luminosities in the 2–10 keV and 1–19 keV band rest frame are  $1.5_{-0.2}^{+0.4} \times 10^{44}$  and  $2.9_{-0.4}^{+0.7} \times 10^{44} \text{ erg s}^{-1}$ , respectively.

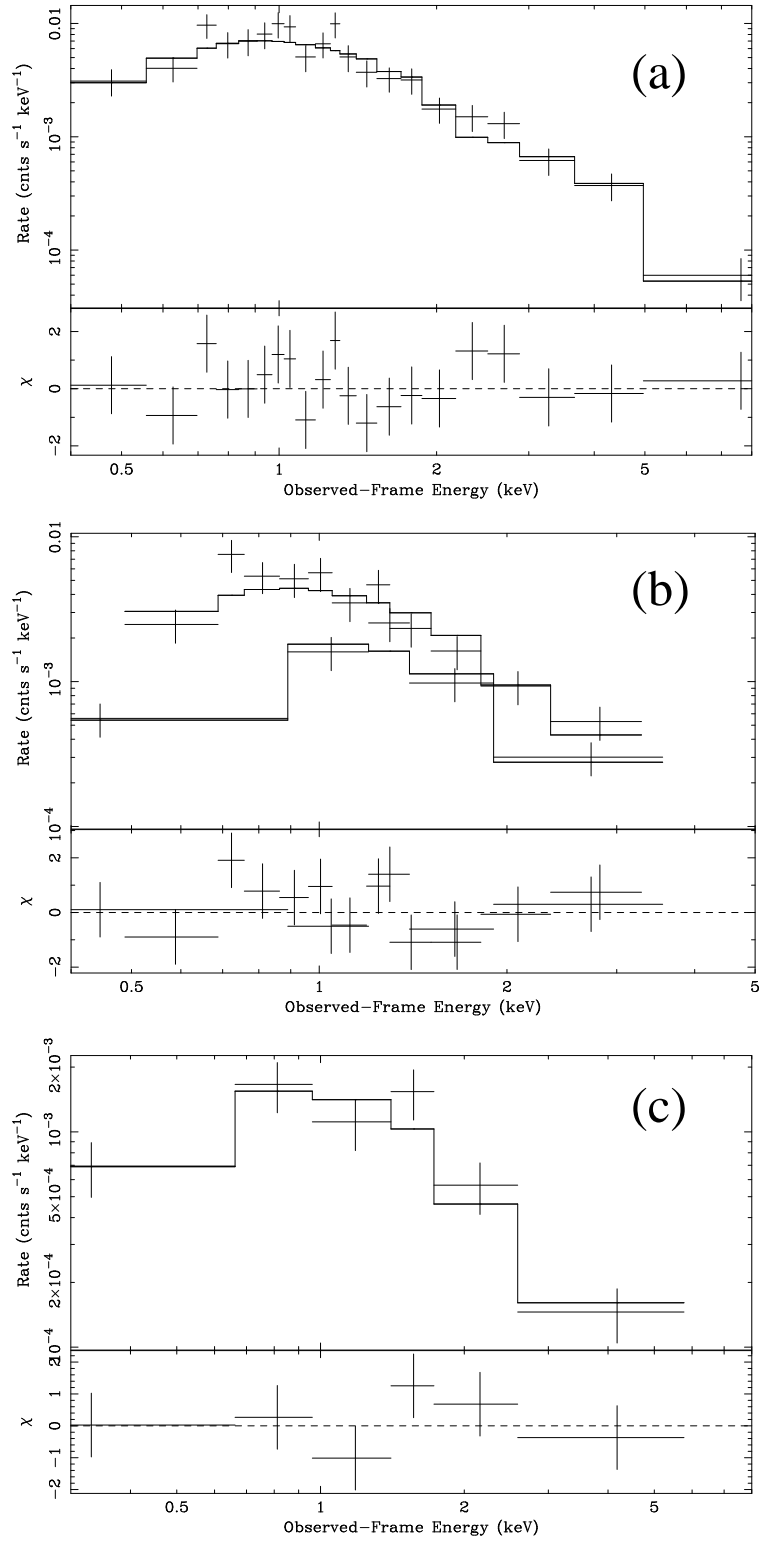


Fig. 2.— *Chandra* spectral fitting results for B1600+434 and B1608+656. (a) The combined spectrum of images A and B of B1600+434. (b) Simultaneous fits to the individual spectra of images A and B of B1600+434. (c) The combined spectrum of all images of B1608+656.

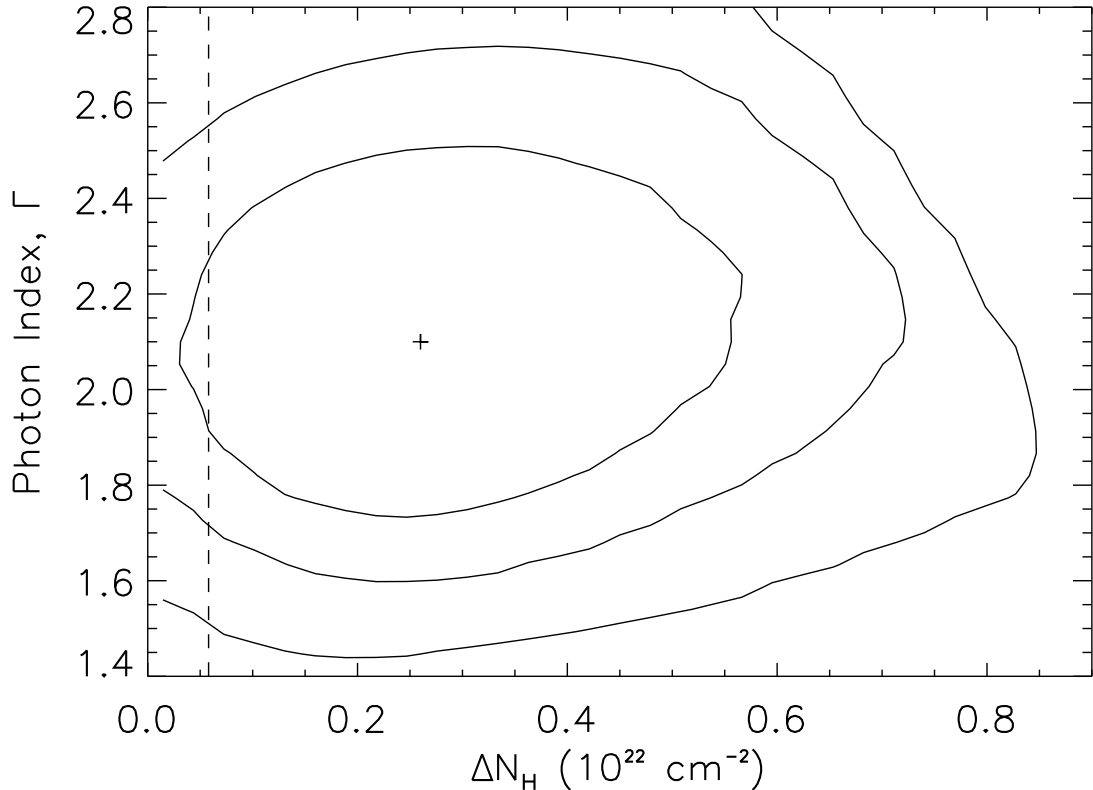


Fig. 3.— 68%, 90% and 99% confidence contours on the photon index and the differential absorption column density  $\Delta N_{\text{H}}$  at the lens ( $z = 0.41$ ) between images A and B of B1600+434. The differential absorption is detected at approximate 90% confidence. The dashed line indicates the differential absorption expected from the differential extinction of  $\Delta E(B-V) = 0.1$  mag between images A and B (Falco et al. 1999) and assuming a standard dust-to-gas ratio of  $5.8 \times 10^{21} \text{ mag}^{-1} \text{ cm}^{-2}$  (Bohlin et al. 1978).

### 3.3. Flux Ratios

We estimated the absorption corrected flux ratio between images A and B of B1600+434 using XSPEC in the 0.4–8 keV band and obtained a flux ratio of  $B/A = 0.57 \pm 0.11$ . We compare this to the time delay corrected flux ratios obtained for the optical and radio bands (Koopmans et al. 2000; Burud et al. 2000) in Table 2. For B1608+656 we estimated the flux ratios based on the image count rates because of the low S/N of individual images. In addition, we estimated the count rate of combined images A and C since it is difficult to resolve the two images. The result for B1608+656 is listed in Table 3. The flux ratios in X-rays are consistent with the time delay corrected flux ratio in the radio band in B1608+656 (Fassnacht et al. 1999).

## 4. Cluster Analysis

It is important to constrain the mass and central location of any nearby groups or clusters to construct a better lens model. We performed source detection on the two *Chandra* observations over the full ACIS fields using the CIAO tool `wavdetect` (Freeman et al. 2002) provided by CXC and did not find significant extended X-ray emission in either field. We also smoothed the image with the `csmooth` (Ebeling, White, & Rangarajan 2000) software tool to detect any extended sources within 4' of the lens galaxies in the ACIS-S3 and S2 fields in both observations. We removed the point sources detected by `wavdetect` before the smoothing process. However, the smoothed images do not show significant (above  $3\sigma$ ) extended emission close to the lens galaxies in either field. We also smoothed the soft X-ray band images between (0.4–2 keV) to increase the signal-to-noise ratio, as the X-ray emission from the cluster or group is expected to be stronger in the soft X-ray band, and did not find significant extended emission above  $3\sigma$ . We note that there are two low significance extended sources (about  $2.5\sigma$ ) present close the lenses at R.A. =  $16^{\text{h}} 1^{\text{m}} 35^{\text{s}}.9$  and decl. =  $43^{\circ} 17' 27''$  (J2000) with a  $2\sigma$  contour radius of  $\sim 11''$  in the field of B1600+434, and at R.A. =  $16^{\text{h}} 9^{\text{m}} 11^{\text{s}}.3$  and decl. =  $65^{\circ} 32' 7''$  (J2000) with a  $2\sigma$  contour radius of  $\sim 5''$  in the field of B1608+656. However, these sources have low signal-to-noise ratios and could be simply be background fluctuations. In addition, many events in these peaks have energies below 0.4 keV where the calibration uncertainty is large. A longer observation would be required to have any confidence in their existence, so we proceed on the assumption that they are background fluctuations.

We used the background count rates to estimate upper limits on the fluxes of any group/cluster in the two fields. We assumed gas temperature of  $\sim 1$  keV when converting from count rates to flux. This temperature consistent with the upper limits of X-ray luminosities

Table 1. Results of Fits to the *Chandra* Spectra of B1600+434 and B1608+656

Fit	Quasar	Image	$\Gamma$	Galactic $N_{\text{H}}$ ( $10^{20} \text{ cm}^{-2}$ )	Other Absorption $N_{\text{H}}^{\text{a}}$ ( $10^{20} \text{ cm}^{-2}$ )	Flux <sup>b</sup> ( $10^{-14} \text{ erg s}^{-1} \text{ cm}^{-2}$ )	$\chi^2(\nu)$
1	B1600+434	Total	$2.0 \pm 0.2$	$14 \pm 4$	...	$6.8 \pm 0.9$	16.3(18)
2	B1600+434	Total	$1.9 \pm 0.2$	1.29 (fixed)	$90 \pm 40$ ( $z = 1.59$ )	$6.8 \pm 1.0$	16.1(18)
3	B1600+434	Total	$1.9 \pm 0.2$	1.29 (fixed)	$22 \pm 8$ ( $z = 0.41$ )	$6.8 \pm 1.2$	15.8(18)
4 <sup>c</sup>	B1600+434	A	$2.1 \pm 0.2$	1.29 (fixed)	$21 \pm 11$ ( $z = 0.41$ )	$3.6 \pm 0.7$	13.1(12)
		B			$47^{+21}_{-17}$ ( $z = 0.41$ )	$1.8 \pm 0.6$	
5	B1608+656	Total	$1.4 \pm 0.3$	$< 6.4$	...	$2.3 \pm 0.5$	3.3(3)

Note. — All derived errors are at the 68% confidence level.

<sup>a</sup>Absorption component at the quasar or lens redshift.

<sup>b</sup>Flux is estimated in the 0.4-8 keV observed band without magnification correction.

<sup>c</sup>Simultaneous fits to the individual spectra of images A and B of B1600+434. The two spectra are constrained to have the same intrinsic power-law photon index and Galactic absorption column density but can have different absorption column densities at the redshift of the lens.

Table 2. Flux Ratios of B1600+434

Band	B/A
X-ray (0.4–8 keV)	$0.57 \pm 0.11$
Optical (I) <sup>a</sup>	0.67
Radio (8.5 GHz) <sup>b</sup>	0.825

References. — (a) Burud et al. (2000); (b) Koopmans et al. (2000)

Table 3. Flux Ratios of B1608+656

Band	B/(A+C)	D/(A+C)
X-ray (0.4–8 keV)	$0.4 \pm 0.1$	$< 0.12$
Radio (8.5 GHz) <sup>a</sup>	0.325	0.114

References. — (a) Fassnacht et al. (1999)

obtained from our analysis. The background count rate in the 0.4–2 keV band for B1600+434 is  $5.8 \times 10^{-7}$  count  $\text{s}^{-1}$  arcsec $^{-2}$ . In the analysis, we used an aperture size of 100 kpc radius to limit the effects of any systematic errors in the background estimate. This aperture size is large enough for the groups with luminosities below  $10^{43}$  erg  $\text{s}^{-1}$  (Osmond & Ponman 2004). For a 100 kpc radius at the redshift of the lens ( $z = 0.41$ ), the  $3\sigma$  upper limit of the X-ray flux is  $3.4 \times 10^{-15}$  erg  $\text{cm}^{-2}$   $\text{s}^{-1}$ , which corresponds to an X-ray luminosity of  $\sim 2 \times 10^{42}$  erg  $\text{s}^{-1}$ . The background flux in the 0.4–2 keV band for B1608+656 is  $5.3 \times 10^{-7}$  count  $\text{s}^{-1}$  arcsec $^{-2}$ . For a 100 kpc radius at the redshift of the lens ( $z = 0.63$ ), the  $3\sigma$  upper limit of the X-ray flux is  $3.5 \times 10^{-15}$  erg  $\text{cm}^{-2}$   $\text{s}^{-1}$ , which corresponds to an X-ray luminosity of  $\sim 6 \times 10^{42}$  erg  $\text{s}^{-1}$ .

We used the standard  $L_X$ – $T_X$ ,  $\sigma$ – $T_X$ , and  $\sigma$ – $L_X$  relations (e.g., Girardi et al. 1996; Helsdon & Ponman 2000; Xue & Wu 2000; Mahdavi & Geller 2001; Kochanek et al. 2003; Osmond & Ponman 2004) for groups and clusters to estimate upper limits for the velocity dispersion of any cluster of  $\sigma \sim 400$  and  $\sim 500$  km  $\text{s}^{-1}$  for B1600+434 and B1608+656 respectively. The large scatter of the relations were considered when estimating the upper limits. Considering a singular isothermal sphere model for the group or cluster, the lens potential,  $\phi$ , from the group/cluster is

$$\phi = 4\pi \left(\frac{\sigma}{c}\right)^2 \frac{D_{LS}}{D_{OS}} r = br, \quad (1)$$

where  $D_{LS}$  and  $D_{OS}$  are angular diameter distances from the lens to source and observer to source, and  $r$  is the angular distance from the lens to the group/cluster. Thus, the lens strength,  $b$ , is constrained to have upper limits of  $b \lesssim 3''.0$  and  $\lesssim 3''.2$  for B1600+434 and B1608+656 respectively.

## 5. Serendipitous Sources

We also cataloged the serendipitous point sources in the two fields using the CIAO tool `wavdetect`. The source detection was performed on each CCD separately with a detection threshold of  $10^{-6}$ . The detection threshold was set as the inverse of the total number of pixels in the binned images. We detected 75 and 82 serendipitous sources in the B1600+434 and B1608+656 fields, respectively. The detection threshold corresponds to a flux limit of roughly  $2 \times 10^{-15}$  erg  $\text{cm}^{-2}$   $\text{s}^{-1}$  and the numbers of sources are consistent with standard estimates for the source numbers at this flux limit (e.g., Cowie et al. 2002, and references there in).

The *Chandra* field of B1600+434 is included in DR3 of the Sloan Digital Sky Survey (SDSS, Abazajian et al. 2004). We searched for optical counterparts of the X-ray sources within a  $2''$  radius, which corresponds to the largest error bars for the *Chandra* positions,

and allows the inclusion of counterparts that have slight offsets between the optical and X-ray centroids, such as the ultra-luminous X-ray sources seen in nearby galaxies. We found counterparts for 27 of the 75 X-ray sources, 13 of which are flagged as quasar candidates in the SDSS catalogs. The properties of the serendipitous sources and the optical counterparts are listed in Table 4.

B1608+656 field is not covered by SDSS, and so we used the Palomar Digital Sky Survey (DPOSS, Djorgovski et al. 2003) survey to identify the counterparts. The lens position in the *Chandra* and DPOSS images are offset by approximately  $1''.5$ , so we used a slightly larger radius to identify optical counterparts. We found 27 optical counterparts out of the 82 X-ray sources. The properties of the serendipitous sources and the optical counterparts in B1608+656 field are listed in Table 5.

## 6. Summary

We present results from *Chandra* observations of the gravitational lenses B1600+434 and B1608+656. We resolved the two lensed images in B1600+434 and three of four images in B1608+656. We did not detect the faintest image D in B1608+656. The analysis of B1608+656 was complicated by the small minimum image separation and the low count-rate of the lensed image D. We could not find a stable solution for the X-ray flux ratios even if we fixed the image positions to those inferred from *HST* observations. A longer observation would be needed to constrain the flux ratios of the individual X-ray images of B1608+656.

We also performed a spectral analysis of the lensed quasar images and detected differential absorption column density of  $\Delta N_{\text{H}} \sim 3 \times 10^{21} \text{cm}^{-2}$  between the two images of B1600+434. The improvement of the fit by allowing differential absorption is significant at the 90% confidence level indicating that the X-ray data are consistent with, but do not require, column density variations. Comparing with the estimated differential extinction of  $\Delta E(B - V) = 0.1$  mag between images A and B (Falco et al. 1999), we obtained a dust-to-gas ratio of  $2.6_{-1.5}^{+1.9} \times 10^{22} \text{mag}^{-1} \text{cm}^{-2}$  within a factor of five from the Galactic value. Considering the patchiness of the interstellar medium, a factor of five difference may not be significant enough to conclude that the dust-to-gas ratio of the lens galaxy in B1600+434 is higher than that of the Milky Way. However, this trend is consistent with the cases in B0218+357 ( $z_l = 0.68$ ) and PKS 1830–211 ( $z_l = 0.89$ , Falco et al. 1999), where the estimated dust-to-gas ratios in the lens galaxies were higher than the Galactic value. It is, however, the opposite of the situation found in Q2237+0305 ( $z_l = 0.04$ , Dai et al. 2003). A larger sample is needed to investigate the average dust-to-gas ratios in high redshift ( $z > 0$ )

galaxies. There is differential extinction in B1608+656 as well, but it is most significant for image D which we failed to detect. Our upper limit on the flux of D is not significant enough to estimate a limit on the dust-to-gas ratio. The differential absorption measured between different images in gravitational lenses may serve as a convenient probe to study the gas content in high redshift galaxies since it can separate the absorbing column originated from the lens galaxy and those intrinsic to quasars.

We did not detect significant X-ray emission from nearby galaxy groups or clusters associated with the lens galaxies. We found upper limits on the X-ray luminosity of any cluster at the lens redshift and within  $4'$  from the lenses of  $\sim 2 \times 10^{42}$  and  $\sim 6 \times 10^{42}$  erg s $^{-1}$  for B1600+434 and B1608+656, respectively. Considering standard cluster relations between X-ray luminosity, temperature, and velocity dispersion and assuming a singular isothermal sphere model for the group/cluster, we obtained upper limits of the lens strength parameter,  $b$ , of  $3''.0$  and  $3''.2$  for B1600+434 and B1608+656 respectively. With such a tight limit, only the poor groups to which each lens belongs could be contributing to the lens potential.

We thank Emilio Falco, Christine Jones, George Chartas, and the anonymous referee for helpful comments. We acknowledge the financial support by *HST* grant GO-9375 and CXC grant GO3-4154X.

Table 4. Serendipitous Sources Detected in B1600+434 Field

Name	R. A. (degree)	Decl. (degree)	R. A. error (")	Decl. error (")	Net Counts	Sig	R. A. optical (degree)	Decl. optical (degree)	D <sub>OX</sub> (")	r* (mag)	SDSS flag
CXO J160022.5+431521	240.09376	43.256002	0.7	0.5	152± 16	13.6	...	...	...	...	...
CXO J160041.2+431544	240.17168	43.262303	1.0	0.8	10± 4	2.8	...	...	...	...	...
CXO J160044.4+430842	240.18509	43.145258	0.6	0.2	26± 7	4.4	...	...	...	...	...
CXO J160045.3+431433	240.18909	43.242736	1.1	0.8	13± 4	3.8	240.18867	43.242565	1.3	22.7490	...
CXO J160047.0+431354	240.19615	43.231796	0.5	0.6	7± 3	2.4	...	...	...	...	...
CXO J160049.2+431433	240.20518	43.242667	0.4	1.0	10± 4	3.3	...	...	...	...	...
CXO J160051.2+431431	240.21355	43.242076	1.0	0.7	26± 6	6.3	...	...	...	...	...
CXO J160053.8+430932	240.22429	43.159003	1.2	0.7	28± 7	5.3	...	...	...	...	...
CXO J160054.8+431528	240.22854	43.258031	0.9	0.4	14± 4	4.6	240.22871	43.257572	1.7	15.9220	...
CXO J160055.4+431052	240.23113	43.181337	0.8	0.5	6± 3	2.4	...	...	...	...	...
CXO J160056.4+431151	240.23515	43.197578	1.0	0.4	9± 3	3.1	...	...	...	...	...
CXO J160100.8+431055	240.25354	43.182145	0.7	0.6	11± 4	3.5	...	...	...	...	...
CXO J160101.6+430108	240.25677	43.019044	2.0	0.8	12± 4	3.5	...	...	...	...	...
CXO J160104.8+431115	240.27041	43.187527	0.9	0.3	8± 3	2.9	...	...	...	...	...
CXO J160105.0+431850	240.27114	43.314013	0.5	0.9	4± 2	1.7	...	...	...	...	...
CXO J160110.8+431139	240.29526	43.194329	0.2	0.1	299± 18	51.1	240.29534	43.193954	1.4	17.1220	TARGET_GALAXY
CXO J160113.2+431803	240.30505	43.300870	0.3	0.2	8± 3	3.4	...	...	...	...	...
CXO J160114.4+430717	240.31025	43.121493	0.8	0.9	9± 4	2.7	...	...	...	...	...
CXO J160116.3+431740	240.31819	43.294634	0.4	0.2	11± 3	4.3	...	...	...	...	...
CXO J160116.8+431834	240.32011	43.309628	0.2	0.3	14± 4	5.7	...	...	...	...	...
CXO J160116.9+431949	240.32073	43.330454	0.5	0.2	10± 3	4.1	240.32050	43.330372	0.7	21.8080	...
CXO J160117.1+432129	240.32156	43.358059	0.4	0.2	53± 8	14.9	...	...	...	...	...
CXO J160120.8+431827	240.33669	43.307585	0.1	0.1	59± 8	22.9	240.33658	43.307536	0.3	20.2470	TARGET_QSO_FAINT
CXO J160121.0+430936	240.33777	43.160101	0.3	0.5	5± 2	2.1	...	...	...	...	...
CXO J160122.8+431522	240.34521	43.256365	0.3	0.2	6± 2	2.7	...	...	...	...	...
CXO J160125.6+431337	240.35703	43.227171	0.2	0.2	3± 2	1.5	...	...	...	...	...
CXO J160125.9+431832	240.35828	43.308986	0.2	0.1	24± 5	11.4	240.35824	43.308991	0.1	21.6330	...
CXO J160126.5+431704	240.36068	43.284556	0.2	0.1	8± 3	3.9	...	...	...	...	...
CXO J160126.6+431313	240.36091	43.220496	0.3	0.2	11± 3	5.0	...	...	...	...	...
CXO J160128.9+430519	240.37078	43.088780	1.0	0.6	11± 4	3.4	...	...	...	...	...
CXO J160129.2+430748	240.37185	43.130045	0.7	0.5	17± 4	5.9	...	...	...	...	...
CXO J160129.5+431940	240.37294	43.327784	0.2	0.2	7± 3	3.4	240.37304	43.327680	0.5	14.1040	...
CXO J160129.8+431533	240.37433	43.259386	0.2	0.1	9± 3	4.3	...	...	...	...	...

Table 4—Continued

Name	R. A. (degree)	Decl. (degree)	R. A. error (")	Decl. error (")	Net Counts	Sig	R. A. optical (degree)	Decl. optical (degree)	D <sub>OX</sub> (")	r* (mag)	SDSS flag
CXO J160130.3+431711	240.37637	43.286424	0.0	0.2	2± 1	1.0	...	...	...	...	...
CXO J160131.1+431814	240.37993	43.304018	0.2	0.2	9± 3	4.1	...	...	...	...	...
CXO J160132.7+431309	240.38644	43.219338	0.1	0.2	5± 2	2.4	240.38645	43.219297	0.2	22.9010	...
CXO J160135.3+431333	240.39740	43.226067	0.1	0.0	330± 18	114.4	240.39737	43.226019	0.2	20.4010	TARGET_QSO_FAINT
CXO J160136.2+431353	240.40113	43.231525	0.1	0.3	4± 2	2.0	...	...	...	...	...
CXO J160136.4+432107	240.40199	43.352020	0.1	0.1	71± 9	28.2	240.40162	43.352124	1.0	22.3800	TARGET_QSO_REJECT
CXO J160137.2+431609	240.40509	43.269321	0.1	0.0	39± 6	18.5	...	...	...	...	...
CXO J160137.3+432236	240.40543	43.376842	0.2	0.2	23± 5	8.5	...	...	...	...	...
CXO J160138.6+432204	240.41088	43.367895	0.4	0.3	6± 3	2.6	...	...	...	...	...
CXO J160141.8+431453	240.42440	43.248288	0.4	0.1	5± 2	2.5	240.42461	43.248106	0.9	20.9150	TARGET_QSO_FAINT
CXO J160141.9+431453	240.42459	43.248073	0.1	0.1	23± 5	11.8	240.42458	43.248080	0.0	20.9290	TARGET_QSO_FAINT
CXO J160143.5+431858	240.43147	43.316195	0.2	0.1	7± 3	3.3	240.43154	43.316113	0.4	25.7410	...
CXO J160143.7+431126	240.43234	43.190683	0.3	0.4	18± 4	7.1	240.43238	43.190730	0.2	23.3230	...
CXO J160144.6+431936	240.43594	43.326831	0.1	0.1	9± 3	4.4	...	...	...	...	...
CXO J160146.4+431419	240.44346	43.238879	0.2	0.3	7± 3	3.5	...	...	...	...	...
CXO J160146.8+431334	240.44529	43.226177	0.1	0.1	223± 15	79.9	240.44533	43.226154	0.1	21.1140	...
CXO J160147.5+430907	240.44803	43.152111	0.6	0.9	12± 4	3.7	...	...	...	...	...
CXO J160147.9+432006	240.44998	43.335108	0.1	0.1	19± 4	8.8	...	...	...	...	...
CXO J160149.6+430836	240.45684	43.143382	0.6	0.3	24± 5	7.0	...	...	...	...	...
CXO J160152.6+430915	240.46947	43.154196	0.5	0.5	49± 8	10.9	240.46913	43.153922	1.3	20.5530	TARGET_QSO_FAINT
CXO J160153.7+431817	240.47391	43.304920	0.0	0.0	510± 23	173.3	240.47392	43.304845	0.3	18.8240	TARGET_QSO_FAINT
CXO J160154.5+431519	240.47735	43.255280	0.3	0.1	3± 2	1.5	240.47692	43.255471	1.3	20.6500	TARGET_QSO_FAINT
CXO J160154.6+431147	240.47791	43.196539	0.5	0.5	6± 3	2.5	...	...	...	...	...
CXO J160154.7+431019	240.47811	43.172163	0.2	0.6	3± 2	1.6	240.47841	43.172037	0.9	22.8610	...
CXO J160156.8+431125	240.48683	43.190556	0.2	0.2	128± 12	32.4	240.48681	43.190463	0.3	19.7180	TARGET_QSO_FAINT
CXO J160158.0+431145	240.49198	43.195840	0.5	0.4	13± 4	5.3	...	...	...	...	...
CXO J160200.1+431228	240.50070	43.207905	0.5	0.3	7± 3	3.3	...	...	...	...	...
CXO J160203.4+431808	240.51433	43.302496	0.2	0.3	3± 2	1.5	...	...	...	...	...
CXO J160203.9+431733	240.51654	43.292745	0.2	0.3	6± 2	3.0	...	...	...	...	...
CXO J160204.2+431558	240.51789	43.266260	0.2	0.2	41± 6	16.8	240.51805	43.265916	1.3	20.7600	...
CXO J160204.3+431556	240.51823	43.265618	0.2	0.1	26± 5	12.2	240.51809	43.265900	1.1	20.9400	...
CXO J160208.0+431357	240.53357	43.232582	0.4	0.3	9± 3	4.1	...	...	...	...	...
CXO J160209.8+431208	240.54096	43.202248	0.5	0.5	9± 3	3.3	...	...	...	...	...

Table 4—Continued

Name	R. A. (degree)	Decl. (degree)	R. A. error (")	Decl. error (")	Net Counts	Sig	R. A. optical (degree)	Decl. optical (degree)	D <sub>OX</sub> (")	r* (mag)	SDSS flag
CXO J160210.8+430500	240.54508	43.083499	0.7	0.6	96± 15	7.5	240.54492	43.083590	0.5	21.1700	TARGET_QSO_FAINT
CXO J160213.0+431212	240.55434	43.203367	0.7	0.5	19± 5	5.4	240.55386	43.203749	1.9	21.2800	TARGET_QSO_FAINT
CXO J160217.9+430659	240.57464	43.116569	0.5	0.4	62± 12	6.4	...	...	...	...	...
CXO J160218.1+430928	240.57562	43.157988	0.8	0.6	62± 9	11.5	...	...	...	...	...
CXO J160221.4+430800	240.58931	43.133401	0.7	0.6	58± 12	5.9	240.58890	43.133187	1.3	22.0480	
CXO J160221.5+431227	240.58993	43.207556	0.8	0.6	21± 5	5.9	...	...	...	...	...
CXO J160221.6+430319	240.59001	43.055445	0.3	0.2	903± 41	30.6	240.59003	43.054918	1.9	17.2630	TARGET_GALAXY TARGET_QSO_CAP
CXO J160232.1+431039	240.63379	43.177725	0.9	0.6	24± 7	4.0	...	...	...	...	...
CXO J160235.5+430813	240.64792	43.136956	0.6	0.5	162± 20	9.9	240.64794	43.137232	1.0	20.8500	TARGET_QSO_FAINT

Table 5. Serendipitous Sources Detected in B1608+656 Field

Name	R. A. (degree)	Decl. (degree)	R. A. error (")	Decl. error (")	Net Counts	Sig	R. A. optical (degree)	Decl. optical (degree)	D <sub>OX</sub> (")	r (mag)
CXO J160713.3+652929	241.80581	65.491391	2.0	0.9	32± 8	4.4	241.80481	65.491737	1.9	21.67
CXO J160719.3+652459	241.83052	65.416517	0.9	0.4	311± 22	22.3	241.83031	65.416038	1.8	19.44
CXO J160727.2+653314	241.86370	65.553915	1.9	1.0	21± 6	4.2	...	...	...	...
CXO J160739.8+652040	241.91592	65.344505	2.2	1.1	20± 6	3.9	...	...	...	...
CXO J160740.4+652817	241.91870	65.471505	0.9	0.4	121± 12	19.8	241.91879	65.470879	2.3	21.82
CXO J160741.5+653017	241.92300	65.504803	2.0	0.6	14± 5	3.6	...	...	...	...
CXO J160747.1+652610	241.94660	65.436200	3.1	0.8	26± 7	5.0	241.94743	65.435570	2.6	21.08
CXO J160803.3+652522	242.01387	65.422904	1.5	0.3	7± 3	2.4	...	...	...	...
CXO J160804.4+652540	242.01872	65.427796	2.0	0.6	14± 5	3.8	...	...	...	...
CXO J160806.5+652204	242.02720	65.367868	2.3	0.4	15± 5	4.2	...	...	...	...
CXO J160807.6+652828	242.03167	65.474558	0.4	0.2	7± 3	2.7	...	...	...	...
CXO J160812.0+652054	242.05015	65.348453	1.7	0.6	12± 4	3.7	242.05020	65.347809	2.3	...
CXO J160813.0+652319	242.05442	65.388855	1.8	0.6	16± 5	4.8	242.05438	65.389442	2.1	21.08
CXO J160816.7+652528	242.06963	65.424496	1.3	0.7	13± 4	4.1	...	...	...	...
CXO J160816.9+652453	242.07071	65.414763	1.7	0.9	10± 4	3.3	...	...	...	...
CXO J160822.0+652245	242.09175	65.379180	1.6	0.7	20± 5	5.2	...	...	...	...
CXO J160823.1+652328	242.09637	65.391192	1.2	0.4	35± 7	8.3	242.09776	65.390694	2.8	...
CXO J160826.7+653546	242.11160	65.596178	1.0	0.2	46± 8	10.5	242.11134	65.595993	0.8	21.84
CXO J160827.3+652445	242.11378	65.412762	0.5	0.2	8± 3	3.4	...	...	...	...
CXO J160831.3+652423	242.13047	65.406416	1.2	0.7	16± 4	5.2	...	...	...	...
CXO J160832.8+652255	242.13706	65.381987	1.3	0.5	11± 4	3.6	...	...	...	...
CXO J160835.1+653605	242.14658	65.601453	0.7	0.3	11± 4	3.9	...	...	...	...
CXO J160835.8+653137	242.14931	65.527038	0.7	0.2	6± 2	2.7	242.15018	65.527252	1.5	16.37
CXO J160836.5+652236	242.15214	65.376812	1.2	0.7	12± 4	3.9	...	...	...	...
CXO J160840.9+653523	242.17070	65.589992	0.7	0.3	9± 3	3.3	...	...	...	...
CXO J160843.8+653245	242.18292	65.546039	0.2	0.1	89± 10	35.4	242.18413	65.545868	1.9	19.86
CXO J160844.1+653246	242.18413	65.546163	0.2	0.1	95± 10	39.3	242.18413	65.545868	1.1	19.86
CXO J160849.1+653358	242.20462	65.566266	0.3	0.1	30± 6	13.4	...	...	...	...
CXO J160850.7+653707	242.21163	65.618791	0.8	0.4	8± 3	3.4	...	...	...	...
CXO J160850.8+653220	242.21187	65.539142	0.1	0.0	617± 25	207.9	242.21214	65.538887	1.0	19.78
CXO J160854.0+653338	242.22506	65.560669	0.4	0.1	12± 3	5.7	...	...	...	...
CXO J160855.0+652738	242.22933	65.460712	0.3	0.3	3± 2	1.5	...	...	...	...
CXO J160858.9+652816	242.24561	65.471199	0.6	0.2	9± 3	4.5	...	...	...	...

Table 5—Continued

Name	R. A. (degree)	Decl. (degree)	R. A. error (")	Decl. error (")	Net Counts	Sig	R. A. optical (degree)	Decl. optical (degree)	D <sub>OX</sub> (")	r (mag)
CXO J160859.4+653225	242.24789	65.540349	0.2	0.0	69± 8	30.0	242.24838	65.540154	1.0	21.07
CXO J160900.4+653445	242.25186	65.579230	0.4	0.1	19± 4	8.7	...	...	...	...
CXO J160901.6+653744	242.25685	65.629054	1.3	0.3	21± 5	6.5	...	...	...	...
CXO J160902.1+653216	242.25881	65.537796	0.7	0.1	4± 2	1.9	...	...	...	...
CXO J160903.9+653040	242.26625	65.511286	0.4	0.2	8± 3	3.6	...	...	...	...
CXO J160904.8+652737	242.27018	65.460319	0.2	0.1	25± 5	11.8	...	...	...	...
CXO J160905.2+653655	242.27176	65.615366	1.0	0.2	13± 4	4.6	...	...	...	...
CXO J160905.5+652400	242.27325	65.400242	1.6	0.4	6± 3	2.3	...	...	...	...
CXO J160906.1+652700	242.27560	65.450274	0.7	0.4	14± 4	5.7	...	...	...	...
CXO J160907.1+653126	242.27985	65.524103	0.3	0.0	6± 2	2.9	242.28047	65.523933	1.1	20.14
CXO J160907.9+652626	242.28297	65.440657	0.5	0.3	16± 4	7.0	242.28284	65.440109	2.0	21.62
CXO J160909.1+652559	242.28817	65.433131	0.8	0.3	6± 2	2.7	...	...	...	...
CXO J160909.6+653252	242.29026	65.547984	0.3	0.1	17± 4	8.1	...	...	...	...
CXO J160911.0+653008	242.29611	65.502295	0.4	0.1	5± 2	2.4	...	...	...	...
CXO J160913.0+653432	242.30456	65.575761	0.2	0.1	92± 10	38.9	242.30478	65.575493	1.0	...
CXO J160913.1+652457	242.30483	65.415846	1.3	0.3	5± 2	2.3	...	...	...	...
CXO J160913.1+653020	242.30487	65.505795	0.3	0.2	6± 2	2.8	...	...	...	...
CXO J160913.4+652827	242.30590	65.474394	0.1	0.1	82± 9	36.7	242.30664	65.474052	1.7	20.42
CXO J160914.1+653700	242.30883	65.616860	0.7	0.3	18± 5	6.5	...	...	...	...
CXO J160914.4+653206	242.31012	65.535131	0.2	0.1	39± 6	17.8	242.31021	65.534958	0.6	...
CXO J160916.8+652852	242.32012	65.481128	0.2	0.1	8± 3	4.1	...	...	...	...
CXO J160917.4+653021	242.32254	65.506092	0.2	0.1	29± 5	13.9	...	...	...	...
CXO J160917.4+652925	242.32268	65.490353	0.0	0.0	2± 1	1.0	...	...	...	...
CXO J160917.7+653104	242.32390	65.517999	0.3	0.1	7± 3	3.4	...	...	...	...
CXO J160919.6+652915	242.33176	65.487717	0.5	0.1	7± 3	3.5	242.33199	65.487556	0.7	18.87
CXO J160919.9+653552	242.33310	65.597953	0.4	0.1	29± 6	11.2	...	...	...	...
CXO J160921.4+652243	242.33930	65.378676	1.4	0.6	11± 4	3.4	242.34024	65.378616	1.4	17.14
CXO J160925.2+653421	242.35506	65.572583	0.1	0.1	36± 6	17.0	...	...	...	...
CXO J160926.6+653844	242.36086	65.645732	0.6	0.2	180± 14	32.6	242.36060	65.645737	0.4	20.59
CXO J160927.2+653247	242.36361	65.546655	0.3	0.1	5± 2	2.4	242.36388	65.546600	0.4	21.39
CXO J160930.8+652810	242.37839	65.469570	0.3	0.0	4± 2	2.1	...	...	...	...
CXO J160936.4+652906	242.40200	65.485094	0.3	0.1	6± 2	3.0	...	...	...	...
CXO J160938.3+653447	242.40970	65.579868	0.2	0.1	79± 9	30.2	242.40987	65.579842	0.3	20.33

Table 5—Continued

Name	R. A. (degree)	Decl. (degree)	R. A. error (")	Decl. error (")	Net Counts	Sig	R. A. optical (degree)	Decl. optical (degree)	D <sub>OX</sub> (")	r (mag)
CXO J160939.7+653235	242.41543	65.543118	0.1	0.1	105± 10	44.3	242.41559	65.542908	0.8	20.73
CXO J160940.1+653313	242.41720	65.553738	0.3	0.0	4± 2	1.9	...	...	...	...
CXO J160941.5+652813	242.42317	65.470465	0.4	0.3	7± 3	3.3	...	...	...	...
CXO J160943.6+653317	242.43203	65.554966	0.4	0.2	16± 4	7.6	242.43243	65.554749	1.0	...
CXO J160943.8+652700	242.43287	65.450271	0.8	0.0	2± 1	1.0	...	...	...	...
CXO J160948.2+653330	242.45110	65.558338	0.6	0.1	6± 2	2.7	...	...	...	...
CXO J160950.9+652922	242.46227	65.489607	0.3	0.0	4± 2	2.0	...	...	...	...
CXO J160953.0+653155	242.47116	65.531966	0.4	0.2	4± 2	1.8	...	...	...	...
CXO J160956.5+652824	242.48574	65.473340	0.9	0.1	7± 3	3.1	...	...	...	...
CXO J160957.6+652129	242.49040	65.358242	0.6	0.2	18± 7	2.8	...	...	...	...
CXO J161001.4+652845	242.50600	65.479256	0.4	0.2	71± 9	24.3	242.50522	65.479378	1.3	18.89
CXO J161004.8+652454	242.52003	65.415231	0.6	0.9	3± 2	1.5	...	...	...	...
CXO J161010.8+652719	242.54515	65.455479	0.4	0.0	5± 2	2.1	...	...	...	...
CXO J161016.6+652354	242.56936	65.398384	1.6	0.8	8± 3	2.7	...	...	...	...
CXO J161029.9+652405	242.62477	65.401536	0.9	0.5	142± 14	17.7	242.62561	65.401230	1.7	20.03
CXO J161052.3+651833	242.71824	65.309300	1.2	0.8	83± 14	7.5	...	...	...	...

## REFERENCES

- Abazajian K., et al. 2004, AJ, submitted, astro-ph/0410239
- Arnaud, K. A. 1996, ASP Conf. Ser. 101: Astronomical Data Analysis Software and Systems V, ed. Jacoby G. & Barnes J., 17
- Bohlin, R. C., Savage, B. D., & Drake, J. F. 1978, ApJ, 224, 132
- Burud, I., Hjorth, J., Jaunsen, A. O., Andersen, M. I., Korhonen, H., Clasen, J. W., Pelt, J., Pijpers, F. P., Magain, P., Østensen, R. 2000, ApJ, 544, 117
- Carter, C., Karovska, M., Jerius, D., Glotfelty, K., & Beikman, S. 2003, ADASS XII ASP Conference Series, Vol. 295, 477
- Chartas, G., Agol, E., Eracleous, M., Garmire, G. P., Bautz, M. W., & Morgan, N. D. 2002a, ApJ, 568, 509
- Chartas, G., Brandt, W. N., Gallagher, S. C., & Garmire, G. P. 2002b, 579, 169
- Chartas, G., Dai, X., Gallagher, S. C., Garmire, G. P., Bautz, M. W., Schechter, P. L., & Morgan, N. D. 2001, ApJ, 558, 119
- Chartas, G., Dai, X., & Garmire, G. P. 2004, in Measuring and Modeling the Universe, Edited by W. L. Freedman (Pasadena: Carnegie Obs.), <http://www.ociw.edu/ociw/symposia/series/symposium2/proceedings.html>
- Chartas, G., Eracleous, M., Agol, E., & Gallagher, S. C. 2004, ApJ, 606, 78
- Chartas, G., Gupta, V., Garmire, G., Jones, C., Falco, E. E., Shapiro, I. I., & Tavecchio, F. 2002c, ApJ, 565, 96
- Cowie, L. L., Garmire, G. P., Bautz, M. W., Barger, A. J., Brandt, W. N., & Hornschemeier, A. E. 2002, ApJ, 566, L5
- Dai, X., Chartas, G., Agol, E., Bautz, M. W., & Garmire, G. P. 2003, ApJ, 589, 100
- Dai, X., Chartas, G., Eracleous, M., & Garmire, G. P. 2004, ApJ, 605, 45
- Dickey, J. M., & Lockman F. J. 1990, ARA&A 28, 215
- Djorgovski, S. G., Carvalho, R. R., Gal, R. R., Odewahn, S. C., Mahabal, A. A., Brunner, R., Lopes, P. A. A., & Kohl Moreira, J. L. 2003, BASBr, 23, 197
- Ebeling H., White D. A., & Rangarajan F. V. N. 2000, MNRAS, submitted

- Falco, E. E., Impey, C. D., Kochanek, C. S., Lehár, J., McLeod, B. A., Rix, H.-W., Keeton, C. R., Munõz, J. A., & Peng, C. Y. 1999, *ApJ*, 523, 617
- Fassnacht, C. D. & Cohen, J. G. 1998, *ApJ*, 115, 377
- Fassnacht, C. D. & Lubin, L. M. 2002, *AJ*, 123, 627
- Fassnacht, C. D., Pearson, T. J., Readhead, A. C. S., Browne, I. W. A., Koopmans, L. V. E., Myers, S. T., & Wilkinson, P. N. 1999, *ApJ*, 527, 498
- Fassnacht, C. D., Womble, D. S., Neugebauer, G., Browne, I. W. A., Readhead, A. C. S., Matthews, K., & Pearson, T. J. 1996, *ApJ*, 460, L103
- Fassnacht, C. D., Xanthopoulos, E., Koopmans, L. V. E., & Rusin, D. 2002, *ApJ*, 581, 823
- Freeman, P. E., Kashyap, V., Rosner, R., & Lamb, D. Q. 2002, *ApJS*, 138, 185
- Gallagher, S. C., Brandt, W. N., Chartas, G., & Garmire, G. P. 2002, *ApJ*, 567, 37
- Garmire, G. P., Bautz, M. W., Nousek, J. A., & Ricker, G. R. 2003, *SPIE*, 4851, 28
- Girardi, M., Fadda, D., Giuricin, G., Mardirossian, F., Mezzetti, M., & Biviano, A. 1996, *ApJ*, 457, 61
- Grant, C. E., Bautz, M. W., Chartas, G., & Garmire, G. P. 2004, *ApJ*, 610, 686
- Helsdon, S. F., & Ponman, T. J. 2000, *MNRAS*, 319, 933
- Jackson, N., de Bruyn, A. G., Myers, S., Bremer, M. N., Miley, G. K., Schilizzi, R. T., Browne, I. W. A., Nair, S., Wilkinson, P. N., Blandford, R. D., Pearson, T. J., & Readhead, A. C. S. 1995, *MNRAS*, 274, L25
- Jackson, N., Helbig, P., Browne, I., Fassnacht, C. D., Koopmans, L., Marlow, D., & Wilkinson, P. N. 1998, *A&A*, 334, L33
- Jaunsen, A. O. & Hjorth, J. 1997, *A&A*, 317, L39
- Keeton, C. R. & Zabludoff, A. I. 2004, *ApJ*, 612, 660
- Kochanek, C. S. 2002, *ApJ*, 578, 25
- Kochanek, C. S. 2003, *ApJ*, 583, 49
- Kochanek, C. S., Falco, E. E., Impey, C. D., Lehár, J., McLeod, B. A., & Rix, H.-W. 1999, in *AIP Conf. Proc.* 470, *After the Dark Ages: When Galaxies were Young (the Universe at  $2 < z < 5$ )*, ed. S. Holt & E. Smith (New York: AIP), 163

- Kochanek, C. S., Keeton, C. R., & McLeod, B. A. 2001, *ApJ*, 547, 50
- Kochanek, C. S., White, Martin, Huchra, J., Macri, L., Jarrett, T. H., Schneider, S. E., & Mader, J. 2003, *ApJ*, 585, 161
- Koopmans, L. V. E. & Fassnacht, C. D. 1999, *ApJ*, 527, 513
- Koopmans, L. V. E., de Bruyn, A. G., Xanthopoulos, E., & Fassnacht, C. D. 2000, *A&A*, 356, 391
- Koopmans, L. V. E., Treu, T., Fassnacht, C. D., Blandford, R. D., & Surpi, G. 2003, *ApJ*, 599, 70
- Mahdavi, A., & Geller, M. J. 2001, *ApJ*, 554, L129
- Morgan, N. D., Chartas, G., Malm, M., Bautz, M. W., Burud, I., Hjorth, J., Jones, S. E. & Schechter, P. L. 2001, *ApJ*, 555, 1
- Mori, K., Tsunemi, H., Miyata, E., Baluta, C., Burrows, D. N., Garmire, G. P., & Chartas, G. 2001, in *ASP Conf. Ser. 251, New Century of X-Ray Astronomy*, ed. H. Inoue & H. Kunieda (San Francisco: ASP), 576
- Myers, S. T., Fassnacht, C. D., Djorgovski, S. G., Blandford, R. D., Matthews, K., Neugebauer, G., Pearson, T. J., Readhead, A. C. S., Smith, J. D., Thompson, D. J., Womble, D. S., Browne, I. W. A., Wilkinson, P. N., Nair, S., Jackson, N., Snellen, I. A. G., Miley, G. K., de Bruyn, A. G., & Schilizzi, R. T. 1995, *ApJ*, 447, L5
- Osmond, J. P. F. & Ponman, T. J. 2004, *MNRAS*, 350, 1511
- Protassov, R., van Dyk, D. A., Connors, A., Kashyap, V. L., & Siemiginowska A. 2002, *ApJ*, 571, 545
- Raychaudhury, S., Saha, P., & Williams, L. L. R. 2003, *AJ*, 126, 29
- Refsdal S. 1964, *MNRAS*, 128, 295
- Snellen, I. A. G., de Bruyn, A. G., Schilizzi, R. T., Miley, G. K., & Myers, S. T. 1995, *ApJ*, 447, L9
- Surpi, G. & Blandford, R. D. 2003, *ApJ*, 584, 100
- Tsunemi, H., Mori, K., Miyata, E., Baluta, C., Burrows, D. N., Garmire, G. P., & Chartas, G. 2001, *ApJ*, 554, 496

Weisskopf, M. C., Brinkman, B., Canizares, C., Garmire, G., Murray, S., & Van Speybroeck, L. P. 2002, *PASP*, 114, 1

Wise, M. W., Davis, J. E., Huenemoerder, Houck, J. C., Dewey, D., Flanagan, K. A., & Baluta, C. 1997, *The MARX 2.0 User Guide*, CXC Internal Document

Xue, Y.-J., & Wu, X.-P. 2000, *ApJ*, 538, 65